Compact lens-based dual-channel adaptive optics scanning laser ophthalmoscopy for *in-vivo* three-dimensional retinal imaging in mice

Zhongqiang Li [a], Stella Mary [a], Thomas V Johnson [a,*], Ji Yi [a, b, *]

[a] Department of Ophthalmology, Johns Hopkins Medicine, Baltimore, Maryland, United States

[b] Department of Biomedical Engineering, Ophthalmology, Johns Hopkins University, Baltimore, Maryland, United States

Corresponding authors:

* Thomas V Johnson, Email: johnson@jhmi.edu; Ji Yi, E-mail: jiyi@jhu.edu.

Abstract:

Adaptive optics (AO) has been instrumental in ophthalmic imaging, by correcting wavefront aberrations in ocular optics and achieving diffraction-limited resolution. Current state-of-the-art AO retinal imaging systems use mirror-based optics to avoid surface reflection and chromatic aberrations, requiring a large system footprint with long focal length spherical mirrors. Here we report a compact refractive lens-based AO scanning laser ophthalmoscopy (SLO) system with simultaneous dual-channel fluorescence imaging capacity in mouse retina. The optical layout fits on a 2'x2' optical breadboard and the whole system is constructed on a mobile 3'x4' optical table. We show that the 3D image resolutions are significantly improved with AO correction, particularly in the z-axis (2x improvement compared to without AO, approaching diffraction-limited resolution). The optical design enables survey of a relatively large retinal area, up to 20º field of view, as well as high magnification AO imaging. Simultaneous imaging with 488nm and 561nm laser lines was evaluated using dual-channel AOSLO in CX3CR1-GFP transgenic mice expressing EGFP in microglia, undergoing rhodamine angiography. We performed dynamic high-resolution 3D imaging of microglial morphology every 5 mins for one hour and longitudinally over 3 weeks, demonstrating microglial activation and translocation over short and long time periods in an optic nerve crush model. This lens-based compact AOSLO offers a versatile and compact design for retinal fluorescence imaging in mice.

1. Introduction

The retina is the only noninvasively observable central nervous system tissue. It enables vision by converting light into an electrochemical signal interpretable by the brain and is a critical model system for understanding neural development and neurodegenerative disease states [1]. Advancements in retinal imaging technologies have enabled significant strides in understanding the anatomy and pathology of retinal structure and function [2, 3]. Established retinal imaging methods, such as fundus photography, optical coherence tomography (OCT), and scanning laser ophthalmoscopy (SLO), are limited in resolution by the inherent optical aberrations of the eye [1-4]. To optimize imaging resolution given the maximum numerical aperture (NA) permitted by the pupil, correction of wavefront aberrations are required. Adaptive optics (AO) imaging corrects wavefront aberrations and is capable of capturing details at the sub-cellular level, which enables understanding of retinal anatomy, physiology, pathology and cellular interactions at finer detail than ever before [4-7].

AO technology, originally developed for astronomy, was adapted to ophthalmology to correct optical aberrations induced by the eye's optical imperfections, enabling clearer and more precise imaging of retinal structures [3-7]. AO Scanning Laser Ophthalmoscopy (SLO) achieves ultra-high-resolution imaging of the retina, allowing visualization of individual retinal cells, such as photoreceptors, retinal ganglion cells, and flowing blood cells within capillaries [2, 3, 5, 8-10]. To date, the most common designs for AOSLO systems are mirror-based and use Shark-Hartmann (SH) wavefront sensing (WFS). That design is free of surface reflection as well as chromatic aberration using the off-axis alignment of mirrors, and the wavefront sensing beam wavelength can be independent of imaging beam[7]. However, to reduce the spherical aberration and astigmatism, mirror-based system require large focal lengths (ranging from 375 mm to 1000 mm), which span a large optical footprint [7].

Alternatively, lens-based AOSLO or AOSLO/OCT systems have been designed to permit a more compact system (including even handheld AOSLO devices [11]) while also offering a larger theoretical diffraction-limited field of view [11-20]. However, potential drawbacks include the surface reflections from refractive lenses that confound the wavefront sensing light from the retina, and the chromatic aberrations that render the wavefront distortion wavelength dependent [21]. Computational approaches using sensorless AO have been used to eliminate the need for WFS and overcome both challenges. Optical approaches leveraging polarization have also been successful in rejecting co-polarized surface reflections and retaining only cross- polarized light from the retina for WFS [14]. Using a WFS beam with a wavelength that matches the imaging beam, the chromatic aberration can be somewhat mitigated [14].

Here, we present a lens-based compact AOSLO system that allows simultaneous, volumetric two-color (e.g., 488nm and 552nm) fluorescence imaging in the mouse retina. The system follows the conventional SH scheme and applies polarization optics to remove lens surface reflections. In addition, it utilizes the excitation lasers for WFS to perform AO correction for each channel. The system facilitates a wide field of view (FOV) survey up to a 20º viewing angle which can inform target regions for applying AO correction under higher magnification. We approached the diffraction-limited resolution by the system and demonstrated *in-vivo* imaging performance by fluorescence angiography and dynamic microglial imaging in normal eyes in mice as well as in eyes subject to optic nerve crush.

2. Method

2.1 Lens-based optical design

The schematic of the dual-channel adaptive optics scanning laser ophthalmoscope (DualCH-AOSLO) system is illustrated in Fig. 1a and Supplemental Fig. S1. Briefly, two laser lines (Coherent, 488nm and 552nm) are combined and expanded using a dichroic mirror (DC) and a pair of achromatic relay lenses (L1 and L2) with focal lengths of 25 mm and 150 mm. After passing through a polarizing beamsplitter (PBS), the combined laser beams are expanded threefold again to slightly overfill the aperture of the deformable mirror (DM, ALPAO, DM97-15). The laser beam reflected by the DM is demagnified twofold by another pair of achromatic relay lenses (L6 and L7) with focal lengths of 400 mm and 200 mm, conjugating the DM to the tunable lens (TL: ML-20-37, Optotune Switzerland AG). The beam is then further demagnified by lenses L8 and L9 (focal lengths: 150 mm and 100 mm) to match the 10-mm galvanometer scan mirrors and relay TL to the fast galvanometer mirror. Two slow galvanometer mirrors (GM1 and GM2) (Thorlabs Inc, 6215H), operating with opposite voltage polarity, project the incident beam to focus on the fast-scanning galvanometer mirror (GM3) [22]. Finally, the fast-scanning mirror is conjugated to the mouse cornea using a pair of lenses (L10 and L11) with focal lengths of 100 mm and 50 mm, compressing the excitation beam to approximately 2.15 mm in diameter. The entire AOSLO system was

installed on a 600 mm-by-600mm breadboard. The detailed layout of the optical system and a photograph are provided in the Supplemental Figs. S1a and S1b.

For fluorescence detection, a 105 μm core multimode optical fiber is used as the pinhole to guide light to the PMT, The equivalent pinhole size is 5.69 times the air disk diameter (ADD) for mouse retinal imaging for the green channel and 4.85 for the red channel. The wavefront sensor is placed behind the PBS to collect the light returning from retina. In order to remove surface reflections from all the lenses, a quarter wave plate (QWP) was placed after the final lens before the mouse eye [14].

The acquisition software was developed in C++ using the Qt platform (Qt Group Inc., USA) for data collection and AO calculations. During data acquisition, fluorescence signals were collected by the PMT and received by the digitizer (ATS9440, Alazar Technologies Inc.). The raw data was then processed and displayed in real-time by the acquisition software. Additionally, our software controls the synchronization of the galvo scanners and the digitizer. For AO calculations and closed-loop operation, the acquisition software integrates the MATLAB Engine to control the WFS and DM.

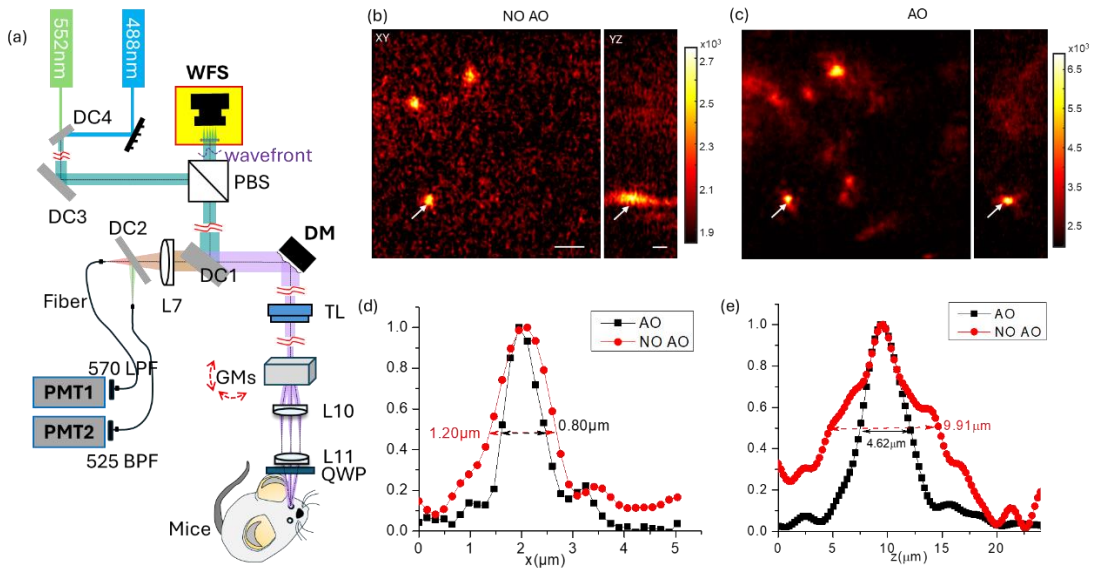

Fig. 1. **System schematic diagram of DualCH-AOSLO and its resolution evaluation with 0.5 μm fluorescence beads.** (a) System schematic diagram of DualCH-AOSLO; (b) and (c) The imaging resolution of 0.5 μm fluorescence beads (red) without AO correction (NO AO) and with AO correction (AO); (d) and (e) The transverse and axial cross section of the fluorescence beads that were used to estimate the lateral and axial imaging resolution before and after AO correction. Scale bar: 5 μm.

2.2 Simulation of imaging plane with changes of DM defocus term

To explore the relationship between the DM defocus term and imaging plane shift in the retina or other objects, optical models using a 3 mm N-BK7 glass ball and a mouse eye model [23] were designed and simulated in Zemax OpticStudio (Ansys, Inc.), as shown in Supplemental Fig. S3. A mathematical model was developed to examine the relationship between the radius R_{WF} of the DM surface arc and the DM surface shift Δd resulting from the defocus Zernike term (Supplemental Fig. S4a).

The R_{WF} was then incorporated into the Zemax model by modifying the DM surface (as illustrated in Supplemental Fig. S4b), and the resulting shifts in the focal plane were recorded by varying R_{WF}. Finally, the relationship between the focal

plane shifts and Δd was established, revealing a linear correlation between these two parameters, as shown in the simulation results in Supplemental Fig. S4c.

2.3 Animal preparation and imaging

All experiments were conducted in accordance with the ethical guidelines for animal care and received approval from the Institutional Animal Care and Use Committee at Johns Hopkins University (Protocol#M021M350). Two C57BL/6J wild-type mice and eight CX3CR1-GFP mice were used in this study. Throughout the imaging process, a mixture of 1% (v/v) isoflurane and oxygen was administered to maintain stable anesthesia, while a heat pad kept the body temperature at 37°C. After the mice were dilated and anesthetized with ketamine/xylazine, 0.1 ml of 2.5% Fluorescein isothiocyanate–dextran (46944-500MG-F, Sigma-Aldrich Co) or 0.1 ml of 2.5% Rhodamine B isothiocyanate–Dextran (R9379-100MG, Sigma-Aldrich Co) was injected retro-orbitally to enable visualization of the retinal vasculature. A +10 D contact lens with hypromellose gel was applied to the cornea to prevent dehydration and cataract formation during imaging. The mice were then positioned on the imaging stage for *in-vivo* retinal imaging using the DualCH-AOSLO. Similar procedures were followed for CX3CR1-GFP mice, but only Rhodamine-B dextran was used for angiography. For AO imaging of fluorescein or GFP, the 488 nm laser was activated for wavefront sensing (552 nm laser for the wavefront sensing during rhodamine angiography), focusing on imaging plane around the inner vascular plexus (IVP) layers by adjusting the TL. The AO closed loop was then initiated to correct for aberrations.

For simultaneous 3D dual-channel data acquisition, both the 488 nm and 552 nm lasers were activated, and a 256 × 256 × 100 image stack was recorded. To study the dynamics of microglial cells, imaging fields containing 1 to 4 cells in the superficial vascular plexus (SVP) layers were selected, and TL was adjusted to confirm the morphology of microglial cells in the IVP and deep vascular plexus (DVP). During imaging, Rhodamine-B angiography was used to maintain the field of view on the same region of interest, ensuring consistent imaging locations throughout the time-lapse imaging.

To study the dynamics of microglial processes, 0.1 mW of 488 nm laser was used, and the focus plane was shifted to the SVP by adjusting the TL. After opening the AO closed loop and ensuring the Strehl ratio of the wavefront map exceeded 0.8, a 256 × 256 × 50 imaging stack was collected at each time point. Dynamic imaging was repeated immediately after data acquisition and every 5 minutes thereafter. Each dynamic imaging session typically lasted between 35 to 95 minutes for each CX3CR1 mouse, depending on image quality, depth of anesthesia, and animal cooperation.

Optic nerve crush (ONC) surgery was conducted following the procedures described previously [24, 25]. Briefly, mice were anesthetized with isoflurane (as above) and the ocular surface was prepped with 0.5% proparacaine and 5% betadine. A lateral conjunctival incision was made using Vannas scissors and blunt dissection was performed to visualize the optic nerve, taking care not to disrupt the orbital blood circulation. The optic nerve was crushed for 3 seconds using calibrated cross-action forceps. Confirmation of retinal blood flow was made immediately after through direct visualization of the fundus. After ONC , the mouse was imaged on days 1, 2, 3, 8, 10, 14, and 21. On day 21, mice were sacrificed after *in-vivo* imaging, and the retinas were extracted and processed for confocal immunofluorescent microscopy. *Ex-vivo* imaging was performed using a commercial confocal microscope (Zeiss LSM 880 confocal laser scanning microscope, Carl Zeiss Microscopy LLC, White Plains NY).

2.4 Retina dissection and Immunostaining [26]

Mice were humanely euthanized by ketamine/xylazine overdose, followed by cervical dislocation. Under a microscope, a small portion of the eyelid was removed using straight forceps for better visualization. The conjunctiva was held with forceps while micro scissors were used to make small incisions, avoiding damage to the eyeball, optic nerve head, and optic nerve. The extracted eyes were transferred into labeled Falcon tubes containing cold PBS. Eyes were submerged in PBS to facilitate tissue removal and maintain shape. A syringe needle was used to create a small hole at the cornea-sclera junction, followed by a circumferential incision with microscissors to remove the cornea and iris. The lens was gently expelled by pressing on the posterior eyecup. The neural retina was detached and incised radially to create a clover-like shape and transferred onto a membrane with the photoreceptor side down. Retinas were placed in 4% PFA for one hour at 4°C. The fixative was then replaced with PBS, and samples were stored at 4°C until further processing.

Fixed retinal explants were washed in PBS (3 × 5 min) while rocking. Retinas were then incubated in blocking solution (1× PBS, 0.3% Triton X-100, 10% normal goat serum) for 60 min at room temperature with gentle rocking. Retinas were incubated with primary antibodies GFP (ck-1:1000 (GFP 1020 chicken Aves GFP917979), RBPMS-rb-1:500 (1830 rabbit Phosphosolutions NB523r / NB1223y / NB923A), GFAP rt- 1:2000 (2.2B10) 13-300 rat thermo VB298933/ XD346000) diluted in blocking solution (300 µL) for five overnights at 4°C in the dark with rocking. After primary incubation, retinas were washed in PBS (3 × 5 min) and blocked again for 60 min at room temperature. Secondary antibodies (1:1000) were applied in blocking solution (500 µL) and incubated overnight at 4°C in the dark with gentle rocking. Retinas were washed in PBS (3 × 5 min), incubated in DAPI (1:1000 in PBS) for 15 min while rocking, and washed again in PBS for 15 min. Retinas were then transferred onto labeled slides using forceps under a microscope, cover slipped with hard-set mounting media -Aqua-poly/mount-18606-5 from poly science , and stored at 4°C in the dark until imaging. 40X high resolution Imaging was done on the 880 confocal microscope (Zeiss LSM 880 confocal laser scanning microscope, Carl Zeiss Microscopy LLC, White Plains NY.).

2.5 Imaging processing and registration

All images were processed and registered using ImageJ (NIH) and MATLAB (MathWorks Inc). Typically, most volumetric (3D) image stacks exhibited shift artifacts along the Z-axis due to breathing or positional drift of the mouse holder. To eliminate motion-induced artifacts, image registration using a demon-based non-rigid registration algorithm was performed in MATLAB. Subsequently, the image data was smoothed using a Gaussian filter (kernel size: 5x5 pixels).

2.6 Statistics

To quantitatively analyze the dynamics of microglia in different retinal layers, 32 microglial cells from six CX3CR1-GFP healthy mice were selected for analysis. This included 9 cells from the SVP layer, 12 cells from the IVP layer, and 11 cells from the DVP layer. The correlations at each time point for each microglial cell, relative to the initial imaging point (0 min), were used for quantitative comparisons among the three retinal layers. Differences between groups were analyzed using unpaired one-way ANOVA tests in SPSS® 29 software (IBM Inc.). A p-value < 0.05 (*) and p-value < 0.005 (**) were considered statistically significant.

3. Results

3.1 Validation of AO correction

To validate the AO correction, a 3 mm N-BK7 ball lens (Edmund Optics, #43-711) was used to emulate the mouse eye of a similar size and numerical aperture (NA) (as shown in Figs. 1b-c, and Supplemental Fig. S2). A diluted mixture solution

composed of yellow-green (A803431, Polysciences Inc.) and red fluorescent microspheres (A800977, Polysciences Inc.) with a diameter of 0.5 μm were prepared. A small drop of the solution was placed on a piece of lens cleaning tissue and dried. The multimode fiber collecting the signal to PMT was replaced by a 25 μm core fiber, resulting in ADD values of 1.44 for the green channel and 1.9 for the red channel to achieve optimal system resolution.

As shown in Fig. 1c and 1e, the transverse and axial resolutions in the red channel without AO correction (NO AO) were 1.2 and 8.75 μm, respectively. With AO engaged (Fig. 1b and 1d), the system improved to 0.8 and 4.62 μm, a >2-fold improvement in axial resolution, approaching the theoretical diffraction-limited resolutions of 0.73 and 4.91 μm [27]. Similarly, the transverse and axial resolutions in the green channel were 1.21, and 5.40 μm with AO correction (Supplemental Fig. S2a and S2c), in comparison with 1.56 and 10.95 μm without AO correction (Supplemental Fig. S2b and S2d), and 0.64 and 4.29 μm theoretical values [27]. We note that the green channel slightly under performed than the red channel, suggesting that chromatic aberration remained, because the red channel was used when aligning the entire system.

3.2 DualCH-AOSLO angiography retinal imaging

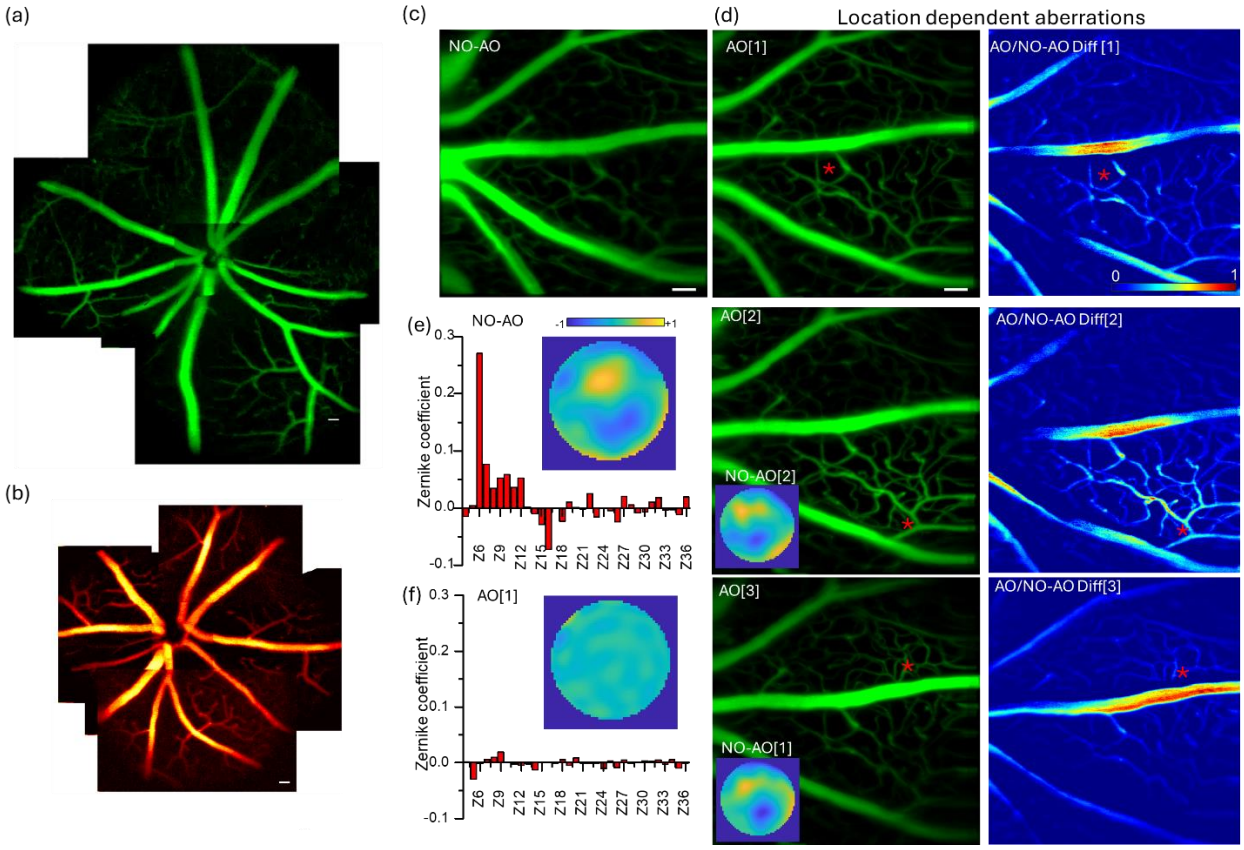

Fig. 2. The Rhodamine-B angiography (RA) and Fluorescein angiography (FA) of DualCH-AOSLO with and without AO correction and their evaluation under large field and small field wavefront sensing. (a) and (b) The extra-large SLO imaging with the conventional angiography. (c) and (d) The MIPs of FA image stacks (1100×1100×100 μm^3) without AO correction and with AO corrections performed at different locations. Red asterisk: center of 200×200 μm^2 WFS area (NO-AO [2] and NO-AO [3] WF maps were inserted in their AO images). (e) and (f) The normalized pixel intensity of AO and NO AO correction under large and small imaging fields in FA. Scale bar: 100 μm.

To survey a large retinal area before engaging AO correction, the system design can acquire up to ~1×1 mm^2 field of view (FOV) by one raster scan, equivalent to a 20° viewing angle. We tested fluorescence angiography by retroorbital injection

of fluorescein dextran (fluorescein angiography, FA) or Rhodamine dextran solutions (Rhodamine angiography, RA) [12]. By stitching several images, an area up to approximately 2.5 × 2.5 mm^2 can be surveyed (Fig. 2a and 2b), which facilitates navigation to a smaller region of interest for high resolution AO correction. Various FOVs for WFS were tested using both RA and FA. With large-FOV WFS (0.8 × 0.8 mm^2, Large field WFS), capillary structures became more distinct with AO imaging compared to non-adaptive optics (NO AO) imaging for both RA and FA (Supplemental Figs. S5a-b). When the FOV was decreased to about 200 × 200 μm^2 (high-magnification WFS), the morphology of single capillaries appeared sharper and clearer with AO correction (Supplemental Figs. S5a and S5c) as compared to NO AO images (Supplemental Figs. S5b and S5d). In both large-FOV and zoom-in FOV WFS, the normalized pixel intensity revealed that AO imaging improved the signal values by ~2x compared with NO AO imaging (Supplemental Figs. S5e-h).

Meanwhile, according to existing literature, field-dependent aberrations may also be introduced when the mouse eye is positioned off-axis relative to the AOSLO system [12]. A FOV without AO correction was recorded and is shown in Fig. 2c, where most of the capillary structures are not clearly visible. Next, we performed AO corrections at different locations within the superficial plexus of the FOV (Fig. 2d, left column, with WF areas marked by red asterisks) and compared their performance. Compared to the NO-AO image, capillary structures were significantly improved at the AO[1] location, where the WF area was positioned near the center of the FOV. When the WF areas were moved to the bottom-right corner (AO[2]) or the top-left corner (AO[3]), the regions where WF sensing was performed appeared relatively brighter, and the capillary features became clearer than in the no WF sensing condition. The 'AO/NO-AO' difference (right column in Fig. 2d) exhibited a field-dependent signal increase (toward a redder color) at pixels closer to the locations of aberration measurement. Figs. 2e and 2f present wavefront measurements in Zernike modes with and without AO, demonstrating that aberrations were effectively corrected, resulting in a noticeably flatter wavefront map.

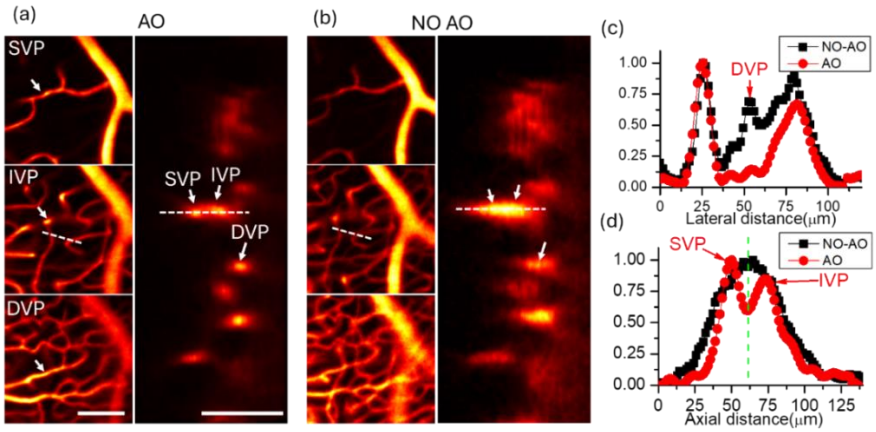

Fig. 3. Characteristics of DualCH-AOSLO for the RA imaging under AO and NO AO imaging. (a) Distinguishing three vascular plexus layers in XY and Z views; (b) the two adjacent capillaries under AO and NO AO imaging in XY view. Scale bar: 100 μm.

We further evaluated volumetric (3D) RA and FA *in vivo*. In *en-face* views of the image stacks, three distinct retinal vascular layers were clearly visible under adaptive optics (AO) imaging in both RA (Fig. 3a) and FA modes (Supplemental Fig. S6). Along the Z-axis, distinguishing capillary cross-sections in the intermediate vascular plexus (IVP) from those in the superficial vascular plexus (SVP) was challenging without AO imaging (Fig. 3b). However, under AO imaging, these structures became more distinct, improving layer differentiation. This improvement could be quantified from pixel curves along the Z-axis (Fig. 3d). Similar results were observed in FA imaging (Supplemental Fig. S6), confirming the enhanced clarity provided by AO imaging.

Additionally, the IVP and DVP layers were also well identified in both RA and FA under AO imaging. The *en-face* views without AO imaging (Fig. 3b and Supplemental Fig. S6b) could not fully distinguish all IVP capillary features because some DVP capillary features overlapped with those from the IVP. However, this issue was completely resolved after AO correction (Fig. 3a and Supplemental Fig. S6a). These results were further supported by pixel curve analysis in Fig. 3c and Supplemental Fig. S6c.

3.3 Simultaneous 3D in-vivo imaging of GFP-labeled microglia and rhodamine angiography

We then tested simultaneous two-channel AOSLO volumetric (3D) imaging on CX3CR1-GFP mice undergoing RA. RA served as the depth landmark reference for locating microglia (Fig. 4a). *In-vivo* SLO images revealed that microglia cells were distributed throughout the retina, including the nerve fiber layer (NFL), inner plexiform layer (IPL), and outer plexiform layer (OPL), corresponding to SVP, IVP, and DVP layers (Fig. 4b and 4c). Notably, a greater density of microglia was observed in the IVP and DVP layers compared to the SVP layer. With AO correction, the processes of microglia became sharper across all three vascular layers with small branches distinctly visible (Fig. 4b). Most microglia retained a ramified shape. In contrast, imaging contrast was poor under NO AO conditions; the processes of microglia appeared blurred, and small process branches were not observable (Fig. 4c). Additionally, microglial morphologies (commonly used to ascertain the activation state) could not be reliably determined from the NO AO SLO images. The RA imaging revealed that the IVP layer blended with the DVP later under NO AO imaging (Fig. 4c); and in contrast, it was distinctly visible with AO correction (Fig. 4b).

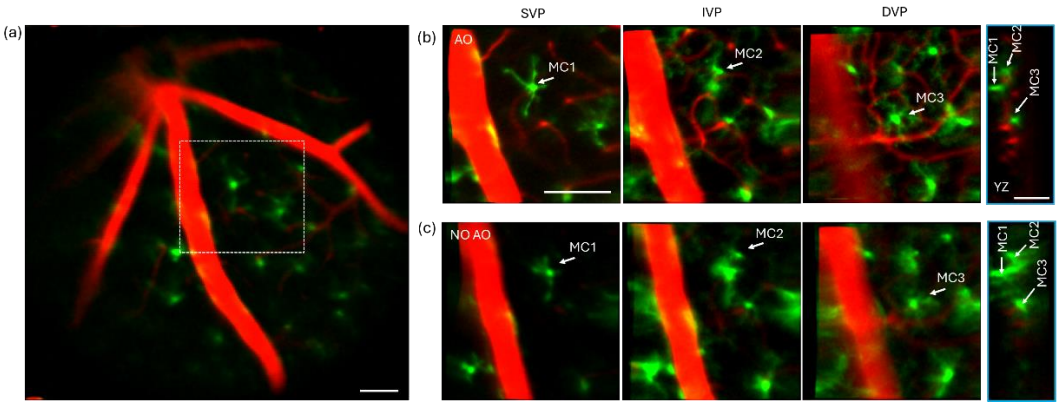

Fig 4. *In-vivo* 3D imaging of microglia cells composited with angiography under the AO and NO AO imaging. (a) Large field conventional SLO images of MCs composited with RA imaging. (b) Three MCs layers distribute along with the three vascular plexus layers under AO imaging; (c) Three MCs layers distributed along with the three vascular plexus layers under NO AO imaging. Scale bar: 100 μm.

In-vivo 3D AOSLO imaging allowed us to clearly visualize the intricate processes of ramified microglia, enabling the monitoring of microglial dynamics across three retinal layers, as shown in Fig. 5 and Supplemental Figs. S7. We imaged a healthy eye every 5 minutes over one hour. At baseline, we observed the initial expansion of two major processes, along with several small branches (Fig. 5a). These processes began retracting toward the cell body after 5 minutes, with a velocity of approximately 3.43 ± 0.19 μm/min. The lower process continued to retract slightly after 20 minutes. Over the course of 60 minutes, three new branches emerged from the microglial cell, while the top major branch disappeared completely. In contrast, most ramified microglia in the deeper retinal layers (IPL and OPL) showed minimal to no change during the extended imaging period, as depicted in the images in Figs. 5b and 5c, as well as in Supplemental Figs. S7b and S7c.

These findings are further supported by the correlation curves for three selected individual MCs (MC1-MC3) over the entire 60-minute imaging period, as shown in Fig. 5d. Each time point was correlated with the starting imaging point (0 min). The SVP layer exhibited relatively lower correlation values, indicating more dynamic morphological changes compared to the deeper layers, while the correlation values for the IVP and DVP layers ranged from 0.95 to 0.98, indicating relatively static morphology (Fig. 5d). Statistical analysis of 32 MCs from all three retinal layers revealed that the average correlation for MCs in the SVP layer was 0.897 ± 0.035 (Fig. 5e), which was significantly lower than the correlations for MCs in the IVP and DVP layers (Correlation values: both 0.951 ± 0.016).

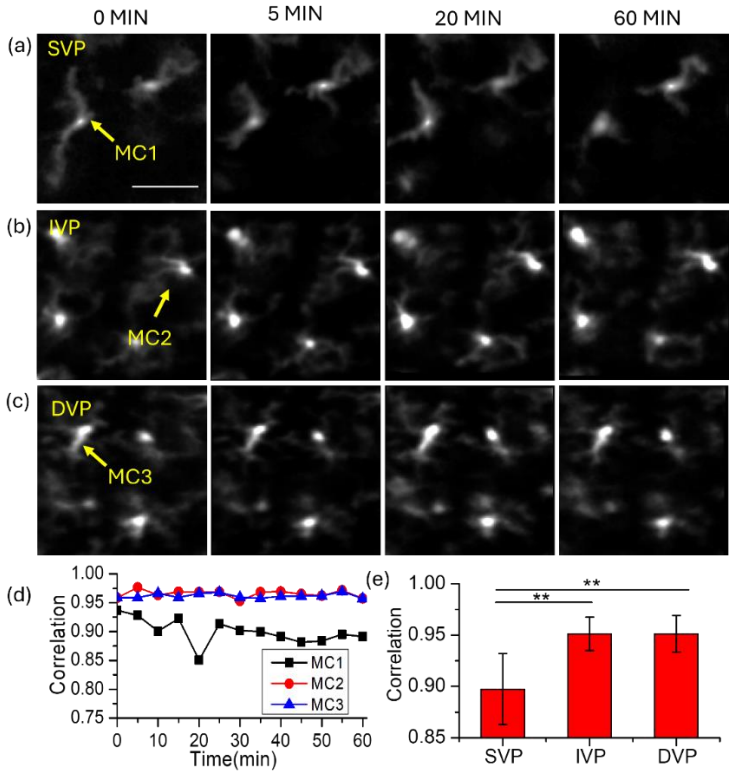

Fig 5. The processes dynamics of MCs under AO imaging. (a-c) MCs with different processes movements at the SVP, IVP and DVP layers. (d) Correlation of individual MC from three different layers at different time points. (e) Correlation of multiple MCs from three different layers among different mice (N= 6 different right eyes, and n= 32 MCs in total). Scale bar: 100 μm.

Finally, we applied DualCH-AOSLO in an ONC mouse model to demonstrate longitudinal activation and accumulation of microglial cells after optic nerve injury[28, 29]. While the morphology of microglia in the SVP showed minimal changes during the first 3 days, both the density and morphology of microglial cells changed significantly after day 8, with fewer processes observed in the SVP (Fig. 6a and Supplemental Fig. S8). By day 21 post-ONC, compared to day 8, radial morphology remained visible in the in-vivo AOSLO images, but the number of microglia had declined (Fig. 6a and 6b). Additionally, microglial cells with more processes were observed in the IVP and DVP at the end of imaging period (Supplemental Fig. S8). Microglia near the optic disk exhibited a distinct radial distribution, with fewer radial cells observed farther from the center (Fig. 6b and Supplemental Fig. S8).

On day 21, the ONC mice were sacrificed, and the fixed retinas were imaged using confocal microscopy (Fig. 6b). The extra-large FOV scanning allowed for clearer observation of the radial morphology of microglia, which was also evident in the *ex-vivo* confocal images (Fig. 6b). In cropped regions of interest (Fig. 6c), three distinct microglia layers were identifiable in both *in-vivo* and *ex-vivo* images, and the SVP layer exhibited a higher density of microglia when compared

to the IVP and DVP layers at 21 days post-ONC (Fig. 6c). Furthermore, compared to the control group, histology revealed that the density of retinal ganglion cells (RGCs) was significantly reduced after 21 days of ONC, with few RGCs detectable in the NFL (Supplemental Fig. S9).

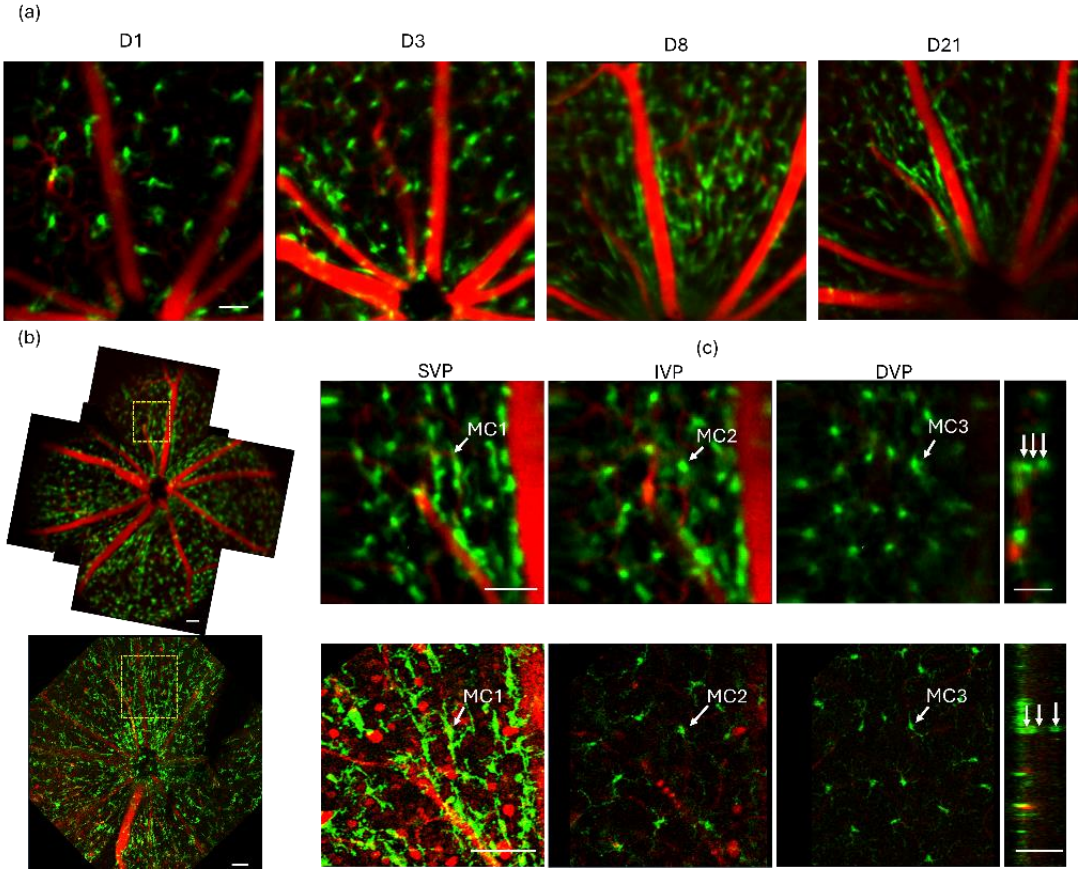

Fig 6. MCs change after optics nerve crush. (a) The *in-vivo* imaging of MCs morphology at SVP on day 1, day 3, day 8, and day 21 after ONC. (b) Wide field of conventional SLO images and its 3D imaging MC morphology on day 21 and compared with *ex-vivo* confocal imaging. Scale bar: 100 μm.

4. Discussion

Recently, lens-based AOSLO systems have emerged as a viable alternative to the mirror-based AOSLO, offering the advantages of a more compact design and a larger theoretical field of view [12, 13]. In this study, we successfully developed a lens-based, compact DualCH-AOSLO system that allows volumetric (3D) simultaneous two-color (e.g., 488nm and 552 nm) fluorescence imaging in the mouse retina. By applying polarization optics incorporating a polarizer and quarter-wave plates, our system effectively reduces back reflections from lens surfaces and minimizes disturbances to wavefront measurements. In AO validation using microspheres, our AOSLO system achieved transverse and axial resolutions of 0.8 μm and 4.62 μm, respectively, in the red channel—closed to the theoretical diffraction-limited resolutions. However, the transverse and axial resolutions in the green channel exceeded the theoretical diffraction-limited resolutions, and this suggests that 488 nm illumination for wavefront sensing remains slightly affected by chromatic aberration. Compared to conventional AOSLO systems, our design is significantly more compact, and AO substantially enhances imaging contrast in angiography.

In mouse models, most AOSLO systems typically achieve a maximum FOV of around 10° by adjusting the scanning angles of the scanners. However, to maintain diffraction-limited performance, these systems often have to operate within a smaller FOV [30-32]. Larger FOVs obtain more imaging features and make it easier to find areas of interest for higher magnification imaging. For other lens-based AOSLO systems [14], although the imaging quality was greatly improved after AO correction, they still attained only small FOV (ranging from 3 to 10°). Compared to these systems, our AOSLO could achieve a much larger FOV (~ 16°) still using AO correction, which resulted in high imaging quality a >2-fold increase in signal to noise ratio. In addition, although the former lens-based design was sensitive to chromatic aberrations, using a bandwidth of about 50 nm, AO performance would not have been significantly influenced by chromatic aberrations [14]. In our setup, we used the excitation laser for WFS, and the wavelength bandwidth between the excitation and emission is around 60-70 nm in RA channel, enabling us to achieve high imaging quality.

In the realm of 3D AOSLO imaging of the retina in mouse models, several studies have successfully demonstrated diffraction-limited performance. However, many of these systems rely on electrically tunable lenses (ETLs) for shifting the imaging plane in the axial direction [12, 13]. This approach is primarily driven by the limited stroke ranges of the deformable mirrors employed in these setups, which restrict their ability to perform effective axial adjustments [12, 13]. Limitations of ETLs include their thermal instability and higher-order aberrations [33]. In this study, our DM had a larger stroke range (up to 40 μm in the defocus mode) that could cover the entire mouse retina. The simulation results indicate that DM shift exhibit a strong linear relationship with changes of the imaging plane in the retina, and it could cover up to 500 μm in the mouse model if using the full 40 μm defocus mode (Supplemental Fig. S4). These results were further verified through angiography imaging, in which we used <50% of stroke ranges to cover all three vascular plexus layers. Compared to NO AO imaging, AO greatly improved imaging contrast (relatively large SNR values) and enhanced the signal intensity by 2x, facilitating resolution of the IVP layer was becoming from the other SVP and DVP layers; two adjacent capillaries could be clearly distinguished from each other under AO imaging.

In this paper, we demonstrated biological significance by imaging microglia cells and their subcellular structure and dynamics. Microglia cells are the predominant immune cells and are strongly believed to play a critical role in inflammatory and degenerative diseases in the brain and the retina [29]. Their morphology serves as an important indicator of their activation state, and therefore of the retina's pathological state [28, 34]. Our DualCH-AOSLO system enabled real-time 3D *in vivo* imaging of microglia, allowing for detailed observation of their behavior, density, and distribution. Using RA imaging as a reference, we identified three distinct layers of microglia: more ramified microglia predominantly located in the IPL, INL, and OPL, which correspond to the IVP and DVP, with fewer microglia were observed in the NFL (corresponding to the SVP). These findings align with existing literature, confirming the accuracy of our imaging approach and providing valuable insights into microglial distribution in the retina [28, 29, 34, 35]. In addition, we performed simultaneous two-color fluorescence imaging in this experiment. Although the 488 nm excitation laser was used for WFS, imaging quality significantly improved in both channels after AO correction. The three vascular layers and microglial layers were well aligned in the Z-view. This result suggests that AO can also mitigate the effects of chromatic aberration, enhancing imaging quality during two-color imaging.

Similar to the enhancements seen in angiography imaging, the AO imaging in our DualCH-AOSLO system significantly improves the visualization of the fine branches and morphology of microglia. This level of detail is crucial, as understanding microglial dynamics is essential to understanding in fine detail and temporal resolution how microglia respond to neurodegenerative insult. By capturing these subtle morphological changes in real time, our system provides

valuable insights into how microglial behavior may contribute to retinal health and pathology, potentially informing future therapeutic strategies [36, 37]. Our setup enables high-resolution 3D imaging of microglial dynamics, allowing for precise observations of their behavior. We measured the average velocity of microglial processes to be approximately 3.43 ± 0.19 μm/min (5-minute step), which is consistent with findings in existing literature. [38, 39]. Additionally, we observed that microglial cells in different retinal locations exhibit varying levels of dynamic process mobility. Specifically, microglia in the SVP layers demonstrated significantly more active process mobility, while those in the IVP and DVP were more static in healthy retinas.

The mouse ONC model has been extensively utilized to study optic neuropathies and central nervous system axon injury and repair, shedding light on the roles and pathological changes of microglia involved in these conditions [29, 40]. Most knowledge about retinal structure and function in these studies is derived from *ex-vivo* experiments, immunohistochemistry of processed tissue, or post-mortem analyses [28, 41]. Conventional *ex-vivo* immunohistochemistry offers exceptional cellular contrast and high resolution of the retina, but it captures information only at a single time point [2]. Because there is a notable lack of *in-vivo* imaging techniques that can dynamically visualize various retinal cell types in their natural environment [42]. In this study, we explored the feasibility of using our setup to monitor microglial morphology following ONC surgery. Our system allows for real-time, 3D *in-vivo* monitoring, providing a more dynamic view of microglial responses to injury in the same location. This capability could enhance our understanding of the temporal changes in microglial morphology and their implications for retinal health and pathology after ONC. Although the morphology of microglia did not show significant changes in the first 3 days after ONC, we observed notable alterations in microglial density. By day 8 post-ONC, microglia exhibited a radial morphology, aligning with our *ex-vivo* confocal images, as well as reported in the literature [28, 29]; when compared to the first 3 days, much less microglia processes were observed from SVP to DVP, which indicated more microglia have been activated after ONC. Unlike existing studies that primarily relied on *ex-vivo* images, we monitored in-vivo microglial morphology in the same mouse up to day 21 after ONC. Radial morphology was still evident at the end of the imaging period, and these findings were further confirmed by confocal ex-vivo imaging. Additionally, we observed that microglial cells exhibited an increased number of processes in both the IVP and DVP at the end of the imaging period. While we used microglial imaging in this study as a proof of principle, this technique could be leveraged to study a number of other relevant cell types in the retina including: RGCs and their dendritic arbors, astrocytes, Muller glia, pericytes, and transplanted neurons.

5. Conclusion

In this study, we introduced a lens-based AOSLO system capable of simultaneous two-color (488 nm and 552 nm) fluorescence imaging in 3D in the mouse retina. Our system follows the conventional SH scheme and incorporates polarization optics to eliminate lens surface reflections. The excitation lasers were also used for WFS, enabling AO correction for each channel. Under AO imaging with a ~16-degree viewing angle, pixel intensities doubled compared to non-AO imaging, enhancing structural differentiation. The IVP layer became more distinct from the SVP and DVP layers, and adjacent capillaries were more clearly distinguishable. For microglial imaging after AO correction, microglial morphology—including fine processes, branching patterns, and distinct layer distributions—was clearly observed. Notably, microglial processes exhibited varying levels of mobility depending on retinal location: those in the SVP layer were more active, while those in the IVP and DVP layers showed less mobility. Following ONC, microglial morphology remained relatively unchanged during the first three days post-injury, but their densities exhibited great alterations. By day 8 post-ONC, microglia adopted a radial morphology. Overall, AOSLO proves to be a powerful tool for investigating early-stage

vascular and neuronal abnormalities associated with retinal diseases with two-color imaging. It provides a unique 3D dynamic view of microglia and their fine processes in their natural environment, offering valuable insights into retinal pathophysiology.

Acknowledgements

We thank the following funding sources supporting this study: NIH R01EY032163, P30EY001765, K08EY031801, R21EY034332, Research to Prevent Blindness (Career Development Award), Bright Focus Foundation G2022005S, The Glaucoma Foundation Rajen Savjani Award, The Shelley and Allan Holt Rising Professorship, and The Zenkel Family Foundation.

6. References

1. Chui, T.Y.P., S. Mo, B. Krawitz, N.R. Menon, N. Choudhury, A. Gan, M. Razeen, N. Shah, A. Pinhas and R.B. Rosen, *Human retinal microvascular imaging using adaptive optics scanning light ophthalmoscopy.* Int J Retina Vitreous, 2016. **2**: p. 11.
2. Mujat, M., R.D. Ferguson, D.X. Hammer, A.H. Patel and N. Iftimia. *High-Resolution Retinal Imaging: Technology Overview and Applications*. in *Photonics*. 2024. MDPI.
3. Bakker, E., F.A. Dikland, R. van Bakel, D. Andrade De Jesus, L. Sanchez Brea, S. Klein, T. van Walsum, F. Rossant, D.C. Farias, K. Grieve and M. Paques, *Adaptive optics ophthalmoscopy: a systematic review of vascular biomarkers.* Surv Ophthalmol, 2022. **67**(2): p. 369-387.
4. Godara, P., A.M. Dubis, A. Roorda, J.L. Duncan and J. Carroll, *Adaptive optics retinal imaging: emerging clinical applications.* Optometry and vision science: official publication of the American Academy of Optometry, 2010. **87**(12): p. 930.
5. Liu, L.X., Z.Q. Wu, M.J. Qi, Y.R. Li, M.L. Zhang, D.Y. Liao and P. Gao, *Application of Adaptive Optics in Ophthalmology.* Photonics, 2022. **9**(5).
6. Geng, Y., L.A. Schery, R. Sharma, A. Dubra, K. Ahmad, R.T. Libby and D.R. Williams, *Optical properties of the mouse eye.* Biomed Opt Express, 2011. **2**(4): p. 717-38.
7. Geng, Y., A. Dubra, L. Yin, W.H. Merigan, R. Sharma, R.T. Libby and D.R. Williams, *Adaptive optics retinal imaging in the living mouse eye.* Biomed Opt Express, 2012. **3**(4): p. 715-34.
8. Scoles, D., Y.N. Sulai, C.S. Langlo, G.A. Fishman, C.A. Curcio, J. Carroll and A. Dubra, *In vivo imaging of human cone photoreceptor inner segments.* Investigative ophthalmology & visual science, 2014. **55**(7): p. 4244-4251.
9. Roorda, A., *Applications of adaptive optics scanning laser ophthalmoscopy.* Optom Vis Sci, 2010. **87**(4): p. 260-8.
10. Roorda, A., F. Romero-Borja, W.J. Donnelly III, H. Queener, T.J. Hebert and M.C. Campbell, *Adaptive optics scanning laser ophthalmoscopy.* Optics express, 2002. **10**(9): p. 405-412.
11. DuBose, T., D. Nankivil, F. LaRocca, G. Waterman, K. Hagan, J. Polans, B. Keller, D. Tran-Viet, L. Vajzovic, A.N. Kuo, C.A. Toth, J.A. Izatt and S. Farsiu, *Handheld Adaptive Optics Scanning Laser Ophthalmoscope.* Optica, 2018. **5**(9): p. 1027-1036.
12. Yang, Y., Q. Zhang, K.J. Cao, W. Chen, S. Paidi, C.-h. Xia, R.H. Kramer, X. Gong and N. Ji, *Retinal microvascular and neuronal pathologies probed in vivo by adaptive optical two-photon fluorescence microscopy.* eLife, 2023. **12**.
13. Qin, Z., S. He, C. Yang, J.S. Yung, C. Chen, C.K. Leung, K. Liu and J.Y. Qu, *Adaptive optics two-photon microscopy enables near-diffraction-limited and functional retinal imaging in vivo.* Light Sci Appl, 2020. **9**: p. 79.
14. Felberer, F., J.S. Kroisamer, C.K. Hitzenberger and M. Pircher, *Lens based adaptive optics scanning laser ophthalmoscope.* Opt Express, 2012. **20**(16): p. 17297-310.
15. Ju, M.J., C. Huang, D.J. Wahl, Y. Jian and M.V. Sarunic, *Visible light sensorless adaptive optics for retinal structure and fluorescence imaging.* Optics letters, 2018. **43**(20): p. 5162-5165.
16. Liang, J.Z., D.R. Williams and D.T. Miller, *Supernormal vision and high-resolution retinal imaging through adaptive optics.* Journal of the Optical Society of America a-Optics Image Science and Vision, 1997. **14**(11): p. 2884-2892.
17. Valente, D., K.V. Vienola, R.J. Zawadzki and R.S. Jonnal, *Kilohertz retinal FF-SS-OCT and flood imaging with hardware-based adaptive optics.* Biomedical Optics Express, 2020. **11**(10): p. 5995-6011.
18. Pandiyan, V.P., X. Jiang, A. Maloney-Bertelli, J.A. Kuchenbecker, U. Sharma and R. Sabesan, *High-speed adaptive optics line-scan OCT for cellular-resolution optoretinography.* Biomedical optics express, 2020. **11**(9): p. 5274-5296.
19. Zawadzki, R.J., P. Zhang, A. Zam, E.B. Miller, M. Goswami, X. Wang, R.S. Jonnal, S.-H. Lee, D.Y. Kim and J.G. Flannery, *Adaptive-optics SLO imaging combined with widefield OCT and SLO enables precise 3D localization of fluorescent cells in the mouse retina.* Biomedical optics express, 2015. **6**(6): p. 2191-2210.
20. Felberer, F., J.-S. Kroisamer, B. Baumann, S. Zotter, U. Schmidt-Erfurth, C.K. Hitzenberger and M. Pircher, *Adaptive optics SLO/OCT for 3D imaging of human photoreceptors in vivo.* Biomedical optics express, 2014. **5**(2): p. 439-456.
21. Merino, D. and P. Loza-Alvarez, *Adaptive optics scanning laser ophthalmoscope imaging: technology update.* Clin Ophthalmol, 2016. **10**: p. 743-55.

22. Shao, W. and J. Yi, *Non-interferometric volumetric imaging in living human retina by confocal oblique scanning laser ophthalmoscopy.* Biomedical Optics Express, 2022. **13**(6): p. 3576-3592.
23. Gardner, M.R.R., H. Grady; Milner, Thomas E. *Computational Model (Zemax) of a Mouse Eye for Visible and Near-Infrared Wavelength Ranges*. 2016 09/17/2023; 04/05/2017:[Available from: https://repositories.lib.utexas.edu/items/c7a0e32c-616c-413a-84c9-8a5003e865aa.
24. Cameron, E.G., X. Xia, J. Galvao, M. Ashouri, M.S. Kapiloff and J.L. Goldberg, *Optic Nerve Crush in Mice to Study Retinal Ganglion Cell Survival and Regeneration.* Bio Protoc, 2020. **10**(6).
25. Heuss, N.D., M.J. Pierson, K.R.C. Montaniel, S.W. McPherson, U. Lehmann, S.A. Hussong, D.A. Ferrington, W.C. Low and D.S. Gregerson, *Retinal dendritic cell recruitment, but not function, was inhibited in MyD88 and TRIF deficient mice.* Journal of Neuroinflammation, 2014. **11**: p. 1-16.
26. Zhang, K.Y. and T.V. Johnson, *Analyses of transplanted human retinal ganglion cell morphology and localization in murine organotypic retinal explant culture.* STAR protocols, 2022. **3**(2): p. 101328.
27. Joel S. Silfies, S.A.S. *The Diffraction Barrier in Optical Microscopy*. [cited 2025 03/05]; Available from: https://www.microscopyu.com/techniques/super-resolution/the-diffraction-barrier-in-optical-microscopy.
28. Yang, P., L. Chen, Y. Shi, F. Zhou, H. Tian, J. Li and L. Gao, *Progesterone alters the activation and typing of the microglia in the optic nerve crush model.* Exp Eye Res, 2021. **212**: p. 108805.
29. Heuss, N.D., M.J. Pierson, H. Roehrich, S.W. McPherson, A.L. Gram, L. Li and D.S. Gregerson, *Optic nerve as a source of activated retinal microglia post-injury.* Acta Neuropathol Commun, 2018. **6**(1): p. 66.
30. Zhang, P., D.J. Wahl, J. Mocci, E.B. Miller, S. Bonora, M.V. Sarunic and R.J. Zawadzki, *Adaptive optics scanning laser ophthalmoscopy and optical coherence tomography (AO-SLO-OCT) system for in vivo mouse retina imaging.* Biomed Opt Express, 2023. **14**(1): p. 299-314.
31. Zhang, P., M. Goswami, A. Zam, E.N. Pugh and R.J. Zawadzki, *Effect of scanning beam size on the lateral resolution of mouse retinal imaging with SLO.* Opt Lett, 2015. **40**(24): p. 5830-3.
32. Terasaki, H., S. Sonoda, M. Tomita and T. Sakamoto, *Recent Advances and Clinical Application of Color Scanning Laser Ophthalmoscope.* J Clin Med, 2021. **10**(4).
33. Grulkowski, I., S. Manzanera, L. Cwiklinski, F. Sobczuk, K. Karnowski and P. Artal, *Swept source optical coherence tomography and tunable lens technology for comprehensive imaging and biometry of the whole eye.* Optica, 2018. **5**(1).
34. Liu, Y., C.M. McDowell, Z. Zhang, H.E. Tebow, R.J. Wordinger and A.F. Clark, *Monitoring retinal morphologic and functional changes in mice following optic nerve crush.* Invest Ophthalmol Vis Sci, 2014. **55**(6): p. 3766-74.
35. Au, N.P.B. and C.H.E. Ma, *Neuroinflammation, Microglia and Implications for Retinal Ganglion Cell Survival and Axon Regeneration in Traumatic Optic Neuropathy.* Front Immunol, 2022. **13**: p. 860070.
36. Zhang, H., C. Tan, X. Shi and J. Xu, *Impacts of autofluorescence on fluorescence based techniques to study microglia.* BMC Neurosci, 2022. **23**(1): p. 21.
37. Stence, N., M. Waite and M.E. Dailey, *Dynamics of microglial activation: a confocal time-lapse analysis in hippocampal slices.* Glia, 2001. **33**(3): p. 256-66.
38. Joseph, A., D. Power and J. Schallek, *Imaging the dynamics of individual processes of microglia in the living retina in vivo.* Biomed Opt Express, 2021. **12**(10): p. 6157-6183.
39. Nimmerjahn, A., F. Kirchhoff and F. Helmchen, *Resting microglial cells are highly dynamic surveillants of brain parenchyma in vivo.* Science, 2005. **308**(5726): p. 1314-1318.
40. Hilla, A.M., H. Diekmann and D. Fischer, *Microglia Are Irrelevant for Neuronal Degeneration and Axon Regeneration after Acute Injury.* J Neurosci, 2017. **37**(25): p. 6113-6124.
41. Wohl, S.G., C.W. Schmeer, O.W. Witte and S. Isenmann, *Proliferative response of microglia and macrophages in the adult mouse eye after optic nerve lesion.* Invest Ophthalmol Vis Sci, 2010. **51**(5): p. 2686-96.
42. Wahl, D.J., P. Zhang, J. Mocci, M. Quintavalla, R. Muradore, Y. Jian, S. Bonora, M.V. Sarunic and R.J. Zawadzki, *Adaptive optics in the mouse eye: wavefront sensing based vs. image-guided aberration correction.* Biomed Opt Express, 2019. **10**(9): p. 4757-4774.